Dispersive coupling between MoSe$_2$ and an integrated zero-dimensional nanocavity

DAVID ROSSER,[1] DARIO GERACE,[2] YUEYANG CHEN,[3] YIFAN LIU,[1] JAMES WHITEHEAD,[3] ALBERT RYOU,[3] LUCIO C. ANDREANI,[2] AND ARKA MAJUMDAR[1,3,*]

[1]*Department of Physics, University of Washington, Seattle, Washington 98195, USA*
[2]*Dipartimento di Fisica, Università di Pavia, 27100 Pavia, Italy*
[3]*Department of Electrical and Computer Engineering, University of Washington, Seattle, Washington 98195, USA*
[*]*arka@uw.edu*

Abstract: Establishing a coherent interaction between a material resonance and an optical cavity is a necessary first step to study semiconductor quantum optics. Here we report on the signature of a coherent interaction between a two-dimensional excitonic transition in monolayer MoSe$_2$ and a zero-dimensional, ultra-low mode volume ($V_m \sim 2(\lambda/n)^3$) on-chip photonic crystal nanocavity. This coherent interaction manifests as a dispersive shift of the cavity transmission spectrum, when the exciton-cavity detuning is decreased via temperature tuning. The exciton-cavity coupling is estimated to be ≈ 6.5 meV, with a cooperativity of ≈ 4.0 at 80 K, showing our material system is on the verge of strong coupling. The small mode-volume of the resonator is instrumental in reaching the strongly nonlinear regime, while on-chip cavities will help create a scalable quantum photonic platform.

1. Introduction

Atomically thin van der Waals (vdW) materials coupled with nanophotonic structures have recently emerged as a promising platform for hybrid integrated photonics [1] due to their easy integration onto a substrate via vdW forces without concern for lattice matching. In particular, the large excitonic binding energy of transition metal dichalcogenides (TMDs) presents an excellent opportunity to study the quantum light-matter interaction in large-scale photonic systems. The first step towards such a quantum system is to demonstrate a coherent interaction between a small mode volume cavity and two-dimensional (2D) TMD excitons. The coherent interaction strength between a cavity and an exciton increases with a large oscillator strength of the excitonic transition and a small mode volume cavity. When the coherent interaction strength is greater than the cavity and exciton losses, the system is said to be in the strong coupling regime. In this regime, the cavity photons and excitons are hybridized into exciton-polariton modes. These polariton modes are generally observed via an anti-crossing between the cavity and the exciton, when one of the resonances is tuned across the other. While strong coupling is necessary to achieve a quantum nonlinearity, for 2D excitons we also need a strong polariton-polariton interaction, which requires the mode-area of the coupled system to be as small as possible [2].

Several research groups have already observed exciton-polaritons using 2D TMD excitons. Plasmonic resonators are an example that have demonstrated impressive room-temperature results [3–6], but are generally lossy (quality factor, $Q \sim 10$) and it is not clear how to create an array of these plasmonic resonators with mutual coupling, an important resource for quantum simulation [7] and strongly correlated photonic devices [8]. Dielectric resonators can provide high quality factors, and researchers have observed exciton-polaritons in TMD excitons using 2D planar cavities, including distributed Bragg reflector (DBR) cavities [9–12] and nonlocal metasurfaces [13]. 1D guided resonances in planar waveguides have also been used to study exciton-polaritons

[14,15]. An advantage of these types of cavities is the strong angular dispersion thanks in part to the lack of 3D confinement of the electromagnetic field. This dispersion allows the investigation of strong coupling via energy-momentum spectroscopy. In other words, by collecting light at different angles of observation from the cavity we can probe different resonance frequencies without the requirement of physically tuning the cavity. However, the lack of 3D confinement also implies large mode-volume and mode-area of the cavities. Hence, it would be difficult to realize a strong polariton-polariton interaction that is inversely proportional to the confinement area [2].

Zero-dimensional (0D) cavities can confine the electromagnetic field in all three spatial dimensions to a sub-wavelength mode volume. As a result of such strong cavity mode localization, the resonance is dispersionless and the exciton-cavity detuning must be modified by some other physical means. Additionally, the small mode-area of 0D cavities allows only a small number of excitons to interact with the cavity, making the light-matter interaction strength smaller. To date, fiber-DBR cavities are the only 0D platform that have demonstrated exciton-polaritons with 2D excitons [16,17]. Here, a fixed DBR mirror and a mechanically movable fiber creates the cavity mode. The cavity length, and hence the cavity resonance frequency, is controlled by the spatial separation of the fiber and bottom DBR. The tuning of the cavity allows for direct observation of the avoided crossing associated with the formation of exciton-polariton modes. Unfortunately, the in-situ tuning advantage of a fiber-DBR cavity comes at the expense of a larger mode volume compared to an on-chip 0D cavity, as well as an unclear path for scaling to a cavity array.

On-chip integrated 0D cavities, such as a photonic crystal defect cavity, provide a means to confine light in a wavelength-scale mode volume while allowing many such cavities to couple to each other via evanescent fields [18]. In fact, TMDs coupled to photonic crystal cavities have already been used to demonstrate optically pumped lasing [19,20], cavity enhanced electroluminescence [21], and second harmonic generation [22,23]. TMD hetero-structures have also been integrated with photonic crystal cavities to demonstrate emission enhancement [24] and lasing [25]. However, no conclusive signature of coherent interaction between TMD excitons and a small mode volume on-chip nanocavity has yet been reported. In fact, such a coherent interaction has never been reported and the value of a coherent light-matter interaction strength g has never been estimated for any 2D excitonic transition, including III-V quantum wells coupled to an on-chip photonic crystal defect cavity. The difficulties lie in the degradation of the quantum well excitonic transition due to etching, lack of in-situ tuning of on-chip cavities, and measuring the 0D cavity in a transmission configuration, where even a small amount of residue from material transfer can suppress optical transmission in a waveguide.

In this paper, we report for the first time the signature of coherent coupling between the neutral exciton in monolayer $MoSe_2$ and a 0D photonic crystal defect cavity made of silicon nitride (SiN). Specifically, we observed a dispersive shift in the cavity transmission spectrum as the exciton is temperature-tuned near the cavity resonance. In the 2D TMD material family, monolayer $MoSe_2$ is the only one with the the neutral exciton as the ground state optical transition [26], and SiN is a standard photonic material transparent at the emission wavelengths of the $MoSe_2$ excitonic transition. By transferring 2D TMD excitons on a pre-fabricated nano-cavity precludes any etching of the excitonic material. We utilized an on-substrate cavity to ensure mechanical stability needed for the 2D material transfer process. Unlike encapsulated SiN nanocavities [27], our on-substrate cavity does not need to be covered with silicon dioxide or a polymer which is important to ensure the cavity resonance does not change with temperature. SiN has a small thermo-optic coefficient which is essential for the temperature tuning experiments reported in this paper, i.e., a bare cavity does not change the resonance frequency under temperature tuning. In comparison, an encapsulating polymer on the cavity can have a significant effect on the cavity resonance [28]. We probe the system under transmission with a cavity red-detuned with respect to the excitonic transition because we found the cavity coupled photoluminescence is affected by

the exciton-phonon interactions [29]. The cavity is measured at large exciton-cavity detunings due to a significant increase in insertion loss of the cavity in transmission at small detunings [30]. Finally, we employed a clean and local dry transfer of 2D materials to ensure no residues are left on the waveguide or gratings [31]. The extracted exciton-cavity coupling from the dispersive shift is $\hbar g \approx 6.5$ meV for an estimated cooperativity $C = 4g^2/(\kappa_0 \gamma_0') \sim 4.0$, in which $\hbar \gamma_0' = 11.11$ meV is the measured broadening of the TMD exciton at 80 K, and $\hbar \kappa_0 = 3.8$ meV is the bare photonic mode linewidth measured without the TMD material. The cooperativity is a measure of the polariton mode splitting visibility, where at $C > 1$ the splitting is greater than the respective linewidths of the upper and lower polariton modes. This shows that our material system is on the verge of strong coupling. The cooperativity can be further enhanced to $C \sim 380$ at 4 K due to reduction of the exciton decay rate and by increasing the cavity quality factor to 10, 000, which is well within the reach of current fabrication technology.

2.   Results

A 0D photonic crystal defect cavity integrated into a waveguide, also known as a nanobeam cavity, was designed (Fig. 1(a)) and fabricated (Fig. 1(b)) in a SiN thin-film on a silicon dioxide substrate with an estimated cavity mode volume $V \sim 2(\lambda/n)^3$, according to the standard cavity QED definition [32]. Three-dimensional Finite difference time domain (3D FDTD) simulations were used to optimize the cavity design [27,33,34] with additional Bragg mirrors included to further improve the cavity quality factor (Appendix A). We note that unlike most SiN photonic crystal cavities, we have an on-substrate, unsuspended cavity. The substrate underneath makes the cavity quality factor lower than what can be achieved in a suspended cavity, but provides the mechanical stability for easy transfer of 2D materials and cleaning of the chip. The bare cavity transmission is interrogated via a confocal microscope using input and output grating couplers, with a $\approx$ 5 μm $\times$ 5 μm collection area and a 5-10% collection efficiency at the cavity resonance frequency. A monolayer $MoSe_2$ flake was then transferred onto the nanobeam via a modified dry transfer method to eliminate any bulk materials or tape residues on the grating or the waveguide [31] (Figs. 1(c), d). This coupled $MoSe_2$-nanobeam device was placed in a cryostat where the temperature was swept between 80 K and 200 K.

2.1.   Device characterization

Monolayer $MoSe_2$ exhibits poor optical contrast on the SiN substrate (Fig. 1(b)). Hence, we confirm the presence of the monolayer on the nanocavity by measuring the photoluminescence (PL) (Appendix A). We observed a strong excitonic peak in the PL spectrum (at 80K), as shown in Fig. 2(a). When the PL is collected from a grating coupler (versus from the full field of view of the confocal microscope), a cavity peak is clearly evidenced in the spectrum (Fig. 2(b)). The background PL is also observed simultaneously due to imperfect spatial filtering in the confocal microscope. Due to a limited field of view in our microscopy setup ($\approx$ 50 μm $\times$ 50 μm), the cavity with transferred monolayer must be in close proximity to the output grating, making the spatial filtering of radiation scattered from the sample difficult.

The nanobeam resonator is characterized via resonant transmission. A broadband supercontinuum laser is directed into one of the gratings and the transmitted radiation is collected from the other grating. Prior to monolayer material integration, the cavity resonance was measured at 300 K to be $\hbar \omega_C = 1595$ meV with a linewidth $\hbar \kappa_0 = 3.8$ meV, corresponding to a bare quality factor $Q_0 = 420$ (Fig. 2(c)). After transfer of the monolayer $MoSe_2$ the bare cavity resonance is measured at 80 K to be $\hbar \omega_C = 1590$ meV with a broadened linewidth $\hbar \kappa = 10.7$ meV, corresponding to a loaded quality factor $Q = 149$ (Fig. 2(d)). The reduction in quality factor is attributed to the optical absorption of the monolayer $MoSe_2$. The shift in the resonance energy primarily comes from the dispersive shift as probed further with temperature tuning. We emphasize that as the linewidth of the monolayer $MoSe_2$ is the dominant source of decay in the
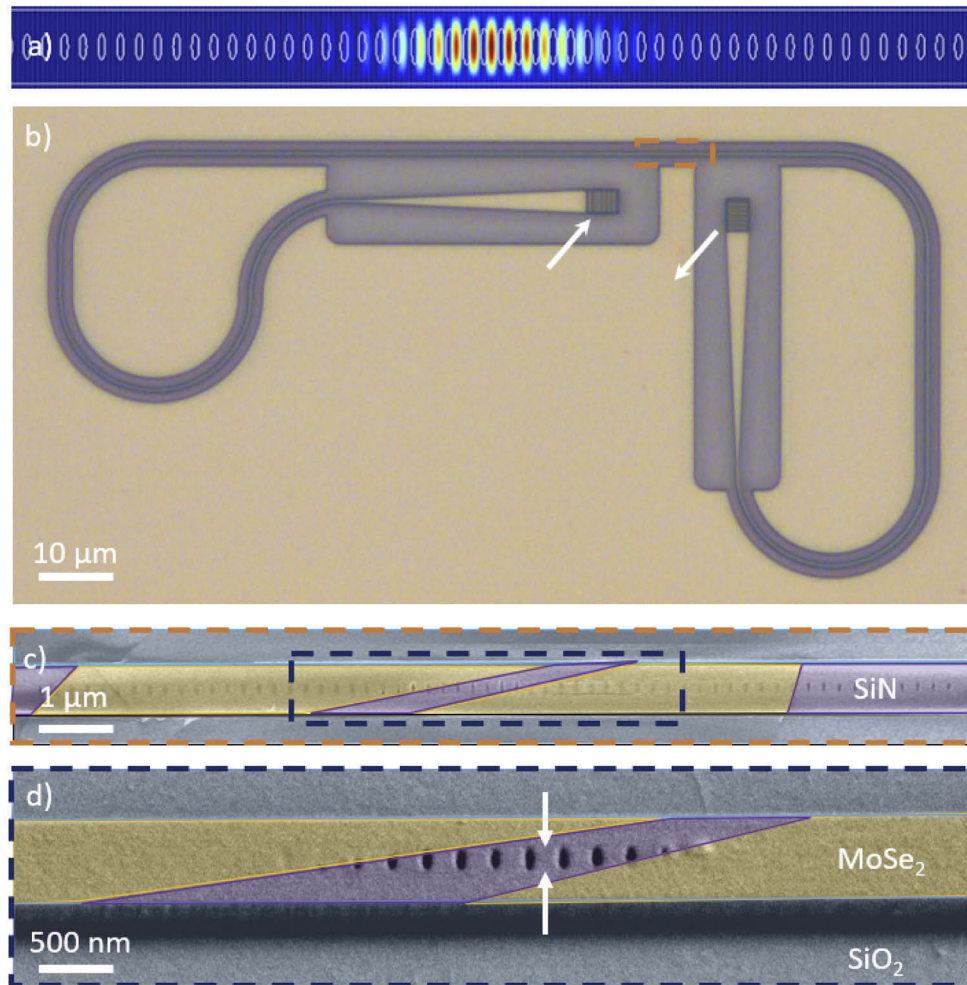
Fig. 1. a) Electric field intensity simulated at the center of the SiN nanobeam cavity by 3D-FDTD at the cavity mode resonance frequency, showing wavelength scale field confinement. The maximum field intensity is seen in the center of the nanobeam. b) Optical image of the monolayer $MoSe_2$ (not visible) integrated onto the nanobeam (orange box) with the inputand output grating couplers (marked by white arrows) for transmission measurements. c) False color SEM image of the monolayer $MoSe_2$ integrated onto the nanobeam. ($MoSe_2$ - gold, SiN - purple, SiO_2 - teal). d) False color SEM image of the monolayer $MoSe_2$ integrated onto the nanobeam with deposited gold to prevent charging. The obstruction of the nanobeam holes is made explicit. White arrows indicate the cavity center.

coupled system, the observed quality factor of the cavity, albeit low, is sufficient to probe the physical effect of coherent coupling.

2.2. Temperature dependence

The neutral exciton PL and cavity transmission were then concurrently measured as the temperature was swept from 80K to 200K. At low temperature, the cavity mode is detuned on the blue side of the excitonic resonance. As the temperature is increased the exciton resonance redshifts, so the detuning between the exciton and cavity resonances decrease. The excitonic PL spectra at
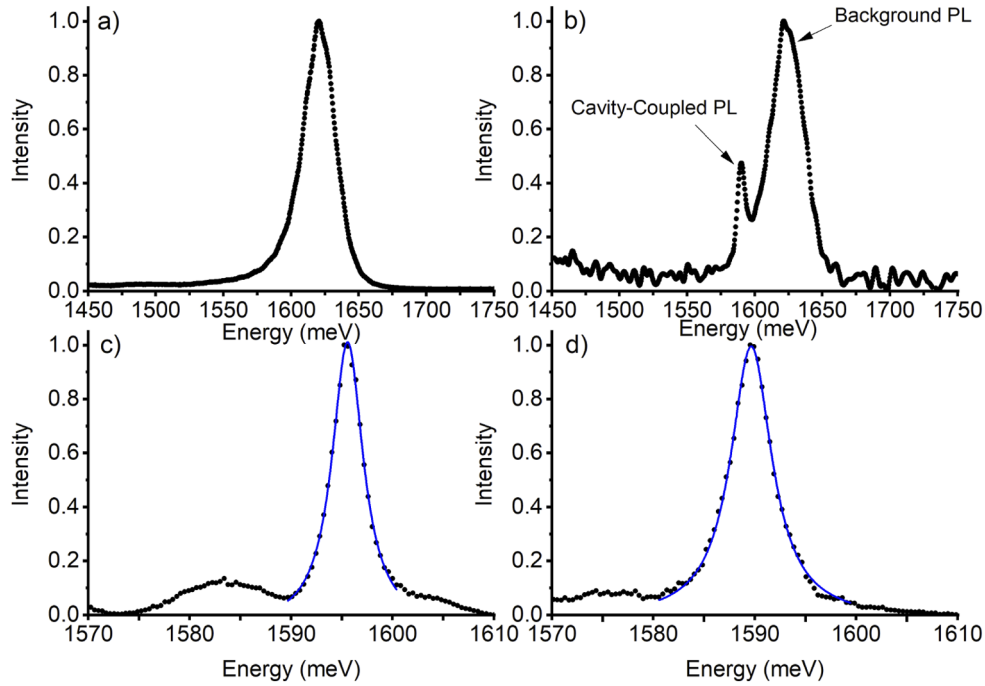
Fig. 2. a) Photoluminescence of monolayer MoSe$_2$ at 80 K. b) Cavity-coupled photoluminescence of monolayer MoSe$_2$ at 80 K. Primary peak is background photoluminescence. Secondary peak is collected from the grating coupler confirming cavity coupling. c) Bare transmission spectrum of the nanobeam cavity at 300 K. The blue curve is a Lorentzian fit to the cavity resonance. d) Transmission spectrum of the nanobeam cavity with an integrated flake of monolayer MoSe$_2$ at 80 K. The blue curve is a Lorentzian fit to the cavity resonance.

different temperatures are fit with a Voigt function [35] to extract the peak energy (ω_X) and linewidth (γ) where we assume the source of inhomogeneous broadening ($\Delta = 4.42 \pm 2.27$ meV) is independent of temperature [36].

The temperature dependence of the neutral exciton peak energy is fit to the standard equation for the semiconductor bandgap [37] (Fig. 3(a)):

$$
\begin{aligned}
E_X(T) &= E_X(0) - S\langle\hbar\omega\rangle[\coth\left[\langle\hbar\omega\rangle/(2k_B T)\right] - 1] \\
&\approx E_X'(0) - 2Sk_B T
\end{aligned}
\tag{1}
$$

where $E_X(0)$ is the zero Kelvin neutral exciton energy, S is a dimensionless coupling constant, and $\langle\hbar\omega\rangle$ is the average phonon energy. This relation corresponds to the neutral exciton energy assuming the exciton binding energy is not strongly temperature dependent. In this experiment, the temperature range explored remains in the linear regime at high temperatures. A fit to the extracted energy of the neutral exciton provides a linearized zero Kelvin neutral exciton energy of $E_X'(0) \equiv E_X(0) + S\langle\hbar\omega\rangle = 1637$ meV and a dimensionless coupling constant $S = 1.21$. These values are comparable to previous reports in the literature [38].

Similarly, the temperature dependence of the neutral exciton linewidth is fit to the Rudin equation [39] (Fig. 3(b)):

$$
\begin{aligned}
\gamma(T) &= \gamma_0 + c_1 T + \frac{c_2}{e^{\Omega/k_B T} - 1} \\
&\approx \gamma_0' + Rk_B T
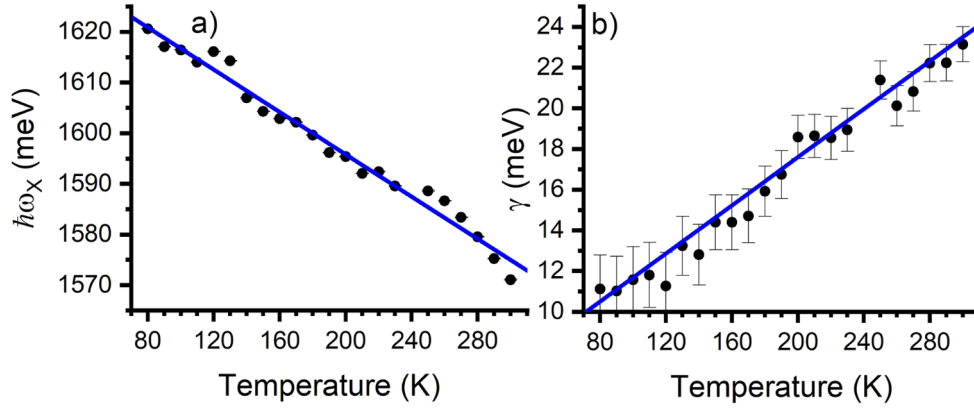\end{aligned}
\tag{2}
$$

Fig. 3. a) Temperature dependence of the neutral exciton resonance. The black dots are the neutral exciton energy observed in the photoluminescence spectrum fit to a Voigt function. The blue line is a fit to Eq. (1). b) Temperature dependence of the neutral exciton linewidth. The black dots are the neutral exciton linewidth observed in the photoluminescence spectrum fit to a Voigt function. The blue line is a fit to Eq. (2).

where γ_0 is the intrinsic homogeneous linewidth, c_1 includes exciton interactions with acoustic phonons, c_2 includes exciton interactions with longitudinal-optical phonons, and Ω is the average phonon energy. In the linearized equation $\gamma_0' = \gamma_0 - \frac{c_2}{2}$ and $R = \frac{c_2}{\Omega}$ where we have assumed $c_1 << c_2$. A fit to the extracted neutral exciton linewidth provides for an intrinsic linewidth of $\hbar\gamma_0' = 5.77$ meV and a dimensionless coupling constant $R = 0.69$. These values are also comparable to previous reports in the literature [36].

It is worth noting the bare nanobeam cavity resonance wavelength does not significantly shift with temperature, which is primarily due to the low thermo-optic coefficient of SiN (Fig. 4(a)). The temperature-independent cavity resonance shift of ~ 5 meV (comparing Fig. 2(a) and Fig. 2(b)) is consistent with the cavity perturbation theory [40,41], where the monolayer material is modelled as a $d = 0.7$ nm thick homogeneous dielectric with an $n_B = \sqrt{\epsilon_B}$ index of refraction where $\epsilon_B = 26$ is the background dielectric constant for monolayer $MoSe_2$ [42]. In the TMD-coupled nanobeam resonator a shift in the cavity resonance is clearly observed as the exciton-cavity detuning decreases (Fig. 4(b)). We attribute this shift to the dispersive coupling of the 2D excitons in the monolayer $MoSe_2$ to the 0D nanobeam cavity mode, which is hereby established via a simple coupled oscillator model. We note that the cavity transmission is significantly suppressed as the exciton is brought into resonance with the cavity (Fig. 5(a)). Additionally, the exciton linewidth increases at higher temperatures precluding the observation of avoided crossing, a hallmark of strong coupling, in the reported system. This is a critical limitation of the temperature tuning. Other tuning mechanisms, such as gas tuning [43], have been considered but the effect of deposited xenon and nitrogen gas on 2D materials leads to inconclusive results.

2.3. Coupled oscillator model

A homogeneous distribution of TMD excitons and a single 0D cavity mode can be phenomenologically modeled with a Hamiltonian describing two coupled oscillators [44,45], wherein the exciton and cavity degrees of freedom coherently interact via an exciton-cavity coupling rate, g. The bare oscillator resonance frequencies are measured with respect to a rotating frame at the resonant driving frequency, ω_L. The full Hamiltonian is

$$H_{XC} = \hbar\Delta_{XL}a^\dagger a + \hbar\Delta_{CL}c^\dagger c + \hbar g(a^\dagger c + c^\dagger a), \qquad (3)$$
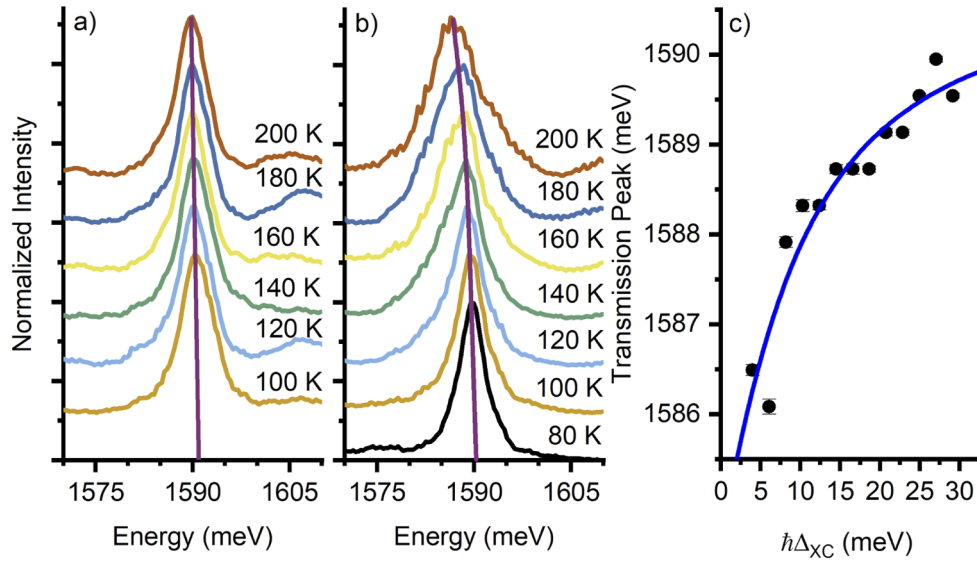
Fig. 4. a) Representative transmission spectra of the nanobeam cavity without an integrated flake of monolayer $MoSe_2$ at 100 K to 200 K in 20 K increments. b) Representative transmission spectra of the nanobeam cavity with an integrated flake of monolayer $MoSe_2$ at 80 K to 200 K in 20 K increments. b) Dispersive shift of the cavity resonance in transmission.
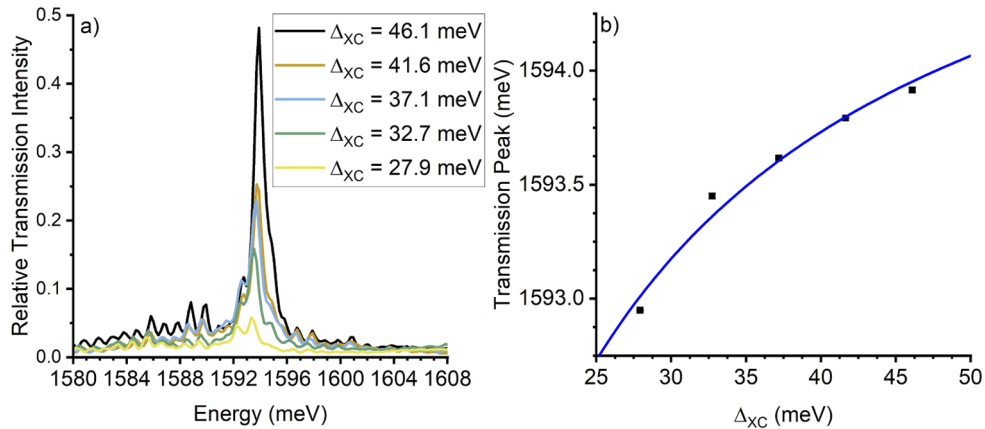

Fig. 5. On a second device: a) Transmission spectra at different exciton-cavity detunings. Note a factor of five reduction in transmission intensity even at large detunings which precludes on-resonance transmission measurements, hence the dispersive regime. b) Dispersive shift of the cavity resonance in transmission for a radiation-matter coupling of $\hbar g = 8.17 \pm 0.36$ meV commensurate with that found in the main device with a different areal coverage.

where $\Delta_{XL} = \omega_X - \omega_L$ and $\Delta_{CL} = \omega_C - \omega_L$ are the detunings of exciton and cavity mode from the laser frequency, respectively; a (c) is the annihilation operator for the exciton (cavity) mode. In the weak excitation regime, exciton saturation and any exciton-exciton interaction can be neglected. Hence, both exciton and cavity operators can be treated as bosonic modes. Including losses, the model can be completed by defining the Liouvillian operator [46] for the density

matrix, $\mathcal{L}(\rho) = \frac{1}{i\hbar}[H,\rho] + \hbar\kappa\mathcal{L}_c(\rho) + \hbar\gamma\mathcal{L}_a(\rho)$, which accounts for the finite cavity and exciton linewidths. The Lindblad operators are $\mathcal{L}_\xi(\rho) = \xi\rho\xi^\dagger - \frac{1}{2}\xi^\dagger\xi\rho - \frac{1}{2}\rho\xi^\dagger\xi$, in which $\xi = a, c$.

By diagonalizing the Liouvillian within the single excitation subspace, the following eigenenergies can be obtained [32,47–49]

$$\omega_\pm = \omega_C + \frac{\Delta_{XC}}{2} - i\frac{\kappa + \gamma}{2} \pm \sqrt{g^2 + \frac{1}{4}\left[\Delta_{XC} + i(\kappa - \gamma)\right]^2}, \tag{4}$$

in which $\Delta_{XC} = \omega_X - \omega_C$ is the exciton-cavity detuning. The experimental data is fit with Eq. (4) for an exciton-cavity coupling energy $\hbar g = 6.47 \pm 0.39$ meV (Fig. 4(b)). Near zero exciton-cavity detuning transmission spectra were not included due to the reduced transmission efficiency inherent to the in-line cavity design [30]. It should be noted the exciton PL peak energy is used as a proxy for the absorption resonance, since $MoSe_2$ is known to have a small Stokes shift [17] which in this case is approximately 1 meV. The extracted light-matter interaction is similar to related nanophotonic structures, although we expect it to be larger with an optimal coverage of the cavity mode [29].

The light-matter coupling energy was numerically simulated, $\hbar g = 4.2$ meV, from a theoretical formulation of the exciton dipole interacting with the cavity mode electric field [50]. We find that g depends on the 2D material extension over the cavity, due to the coupling of a 2D material excitation with a 0D electromagnetic field mode (Appendix B). Qualitative agreement with the value extracted from the dispersive shift is attained when assuming a 2D flake coverage of the nanocavity compatible with the one inferred from the sample SEM (Fig. 1(d)). A maximal simulated exciton-cavity coupling energy $\hbar g = 5.1$ meV is obtained for this cavity design when the 2D flake extension matches the spatial envelope of the cavity mode electric field. We note that our experimentally measured value of $\hbar g$ is slightly larger than the theoretical prediction. We attribute this to less confinement of the electromagnetic field in the cavity due to fabrication imperfections (such as sidewall roughness), and thus a stronger field on the cavity surface than the theoretical design.

3.　Discussion

We have estimated the exciton-cavity coupling strength of a TMD excitonic transition integrated on a 0D SiN nanobeam cavity ($\hbar g = 6.5$ meV) and estimated the cooperativity to be $C \sim 4$, making our material system on the verge of strong coupling. From the known intrinsic linewidth of the neutral exciton of $MoSe_2$ encapsulated in boron nitride (~ 1.7 meV) [51] at 4 K, and an improved cavity quality factor of $Q = 10000$ [27], a cooperativity approaching $C = 4g^2/\kappa\gamma \sim 380$ can be anticipated.

The difficulty remains in the necessary tuning range of the cavity and/or exciton resonance to best observe avoided crossing in this system due to the large linewidth of the excitonic transition. Temperature tuning was used in this paper as it is the only mechanism to provide sufficient range of the exciton-cavity detuning to make observation of a coherent interaction in a dispersionless cavity. The disadvantage to temperature tuning is the increased linewidth of the exciton transition at elevated temperatures preventing the observation of strong coupling. As such, a tunable nanocavity at low temperature is necessary to observe strong coupling with a broad optical transition. The quantum confined Stark effect is a possible in situ mechanism for tuning of the excitonic transition, however the in-plane nature of the intralayer exciton dipole moment with an out-of-plane electric field does not have sufficient tuning range to be practically useful [52]. A hetero-bilayer structure supporting interlayer excitons has a distinct advantage as the excitations then support a dipole moment aligned to an out-of-plane electric field [53]. An alternative form of digital tuning would be to transfer a large-area of monolayer TMDs grown via chemical vapor deposition [54,55] onto an array of nanobeam cavities with different resonant wavelengths. This

would allow for the simultaneous observation of multiple exciton-cavity detunings on many devices.

Surprisingly, the dimensionality mismatch between the 2D MoSe$_2$ exciton and the 0D cavity mode necessitates careful consideration of the spatial dependence of the exciton-cavity coupling. There is a competition between the excitonic envelope function (with the resulting area of the 2D exciton to be minimized) and the cavity field integral (the integrated area should be maximized). This leads to an optimal coverage of the 2D material on the cavity (Appendix B). The primary limiting factor in this coupled system is the TMD neutral exciton linewidth, which can be reduced by boron nitride encapsulation [51]. However, there is a trade-off with a reduced field overlap of the cavity mode with the monolayer material due to the increased physical distance from the cavity field maximum. This problem can be mitigated by using an air mode cavity [56].

A careful review of the published literature reveals limited success in establishing a coherent interaction with monolayer TMDs on nanocavities with negligible dispersion (which includes photonic crystal cavities and ring resonators). We attribute our initial success to a clean transfer method of the monolayer material onto the cavity surface [31]. For example, in this paper we see a bare cavity shift of $\Delta\hbar\omega_C \approx 5$ meV from before and after monolayer transfer. This should be compared to a previous result on a similar device, in which a bare cavity shift of $\Delta\hbar\omega_C \approx 140$ meV was observed [27]. An investigation into a ring resonator device also helped elucidate physics beyond the coupled oscillator model by allowing for simultaneous observation of multiple Δ_{XC} detunings at a given temperature [29]. Reabsorption by the monolayer is expected to be a hindrance as the monolayer is in the same plane as the cavity mode [57]. However, there exist additional phonon-mediated processes, which are detuning and temperature dependent, that must be taken into account. At reduced temperatures there is a marked asymmetry in the observed photoluminescence intensity depending on whether the exciton-cavity detuning is positive or negative. In other words, it is easier to observe cavity-coupled PL with the exciton blue-detuned with respect to the cavity. Furthermore, observations reported in Gebhardt et al. [17], and implicit in the phenomenological model in Rosser et al. [29], indicate the effects of non-Markovian dynamics mediated by polariton-phonon coupling. This effect can be most easily evidenced by the non-Lorentzian lineshape in the transmission spectra at elevated temperatures (Fig. 4(b)). This further manifests itself in the increased uncertainty in precisely determining the cavity linewidth from a Lorentzian fitting function. The difficulties associated with cavity-coupled PL measurements were circumvented by the use of grating couplers to allow for transmission measurements within a standard confocal microscope. Additionally, the far-detuned cavity was chosen in this experiment to ameliorate the effects of absorption and non-Markovian dynamics in transmission measurements to isolate the relevant Hamiltonian parameters.

Note Added: Recently, we became aware of a similar work on a 2D material integrated nanocavity [58].

Appendix A: Materials and methods

Design and fabrication

We followed previously reported design methods for the nanobeam cavity [32,55] to ensure a high quality factor and high transmission efficiency. In the design the mirror strength of the grating (a measure of the grating's reflectivity) is linearly apodized to reduce the out-of-plane scattering from coupling to radiation modes. Note, the out-of-plane asymmetry of our on-substrate cavity, instead of a suspended or an encapsulated cavity, is a non-trivial modification of the design. We first simulated the photonic band diagram via MIT Photonic Bands (MPB) software package [59], and then used the Ansys-Lumerical FDTD electromagnetic solver to optimize the quality factor. The nanobeam is made of a $t = 220$ nm thick and a $w = 779$ nm wide silicon nitride film on silicon oxide substrate. The center region of the nanobeam, where the light is confined, consists of 10 tapering elliptical holes, and the reflectors are made of 20 Bragg mirror holes. The minor

axis radius of the elliptical holes is fixed to 40 nm. The tapering region begins with a 178 nm major axis diameter and a 215 nm center-to-center distance. The tapering region is quadratically tapered to a 121 nm major axis radius and a 233 nm center-to-center distance. The Bragg region remains with fixed values of a 121 nm major axis radius and a 233 nm center-to-center distance. With these design parameters, we obtain a theoretical resonance at 1639 meV, a loaded quality factor of $Q_{loaded} = 11924$, and an intrinsic quality factor of $Q_{intrinsic} = 25480$.

The cavity is fabricated using a 220 nm thick SiN membrane grown via LPCVD on 4 μm of thermal oxide on silicon. The samples were obtained from commercial vendor Rogue Valley Microelectronics. A piece of the wafer is spin coated with roughly 400 nm of Zeon ZEP520A resist. The resist is further coated with a thin layer of Pt/Au which serves as a charge dissipation layer, as both SiN and silicon dioxide are insulators. The resist was then patterned using a JEOL JBX6300FX electron-beam lithography system with an accelerating voltage of 100 kV. The pattern was transferred to the SiN using a reactive ion etch (RIE) in CHF_3/O_2 chemistry. The fabricated sample shows a blue shift of the cavity resonance as compared to the simulated value, as well as significant reduction in the measured Q-factor, which is attributed to fabrication imperfections.

Measurement

The photoluminescence spectrum is measured by exciting the monolayer with a 632 nm Helium-Neon laser. The resulting emission is collected with a free-space confocal microscopy setup following a low-pass filter to remove the excitation laser, and directed into a Princeton Instruments IsoPlane SCT-320 Imaging Spectrograph with a wavelength accuracy of ±0.2 nm. Cavity-coupled photoluminescence spectrum is measured by exciting the monolayer with the same 632 nm Helium-Neon laser and collecting from a grating coupler with the direct photoluminescence emission occluded by a pinhole in the image plane of the confocal microscope. The transmission spectrum is measured by exciting one of the grating couplers with a supercontinuum laser (Fianium WhiteLase Micro) and collecting from the other grating coupler. Using liquid nitrogen in a continuous flow cryostat (Janis ST-500) the energy of the neutral exciton in the monolayer $MoSe_2$ is shifted with consequent changes in the linewidths.

Appendix B: Estimating $\hbar g$ from numerical simulations

In addition to estimating the light-matter interaction by fitting the dispersive cavity shift through the previous expression, a direct calculation for the system under investigation may be obtained by treating the exciton in the 2D TMD layer as a delocalized semiconductor quantum well exciton in a dielectric medium [50], and coupling it to a confined electromagnetic mode. We derive an expression for the radiation-matter interaction in terms of the oscillator strength, f, usually appearing in the Lorentz model for the dielectric response of the 2D material [42], $\varepsilon(E) = \varepsilon_b + f/[E_0^2 - E^2 - i\gamma E]$. The radiation-matter interaction is

$$\hbar g = \frac{\sqrt{df}}{2} \int_\Sigma dx\, dy\ \hat{\epsilon} \cdot \mathbf{E}_{norm}(x, y, z_0) F_{exc}(x, y), \tag{5}$$

in which d is the 2D layer thickness, $\mathbf{E}_{norm}$ is the 2D real electric field at the active material surface (i.e., at z_0), normalized as $\int \varepsilon(\mathbf{r})|\mathbf{E}_{norm}(\mathbf{r})|^2 d\mathbf{r} = 1$, $\hat{\epsilon}$ is a unitary vector selecting the electric field components that are coupled to the dipole transition, F_{exc} is the delocalized exciton envelope function in 2D, and Σ represents the surface over which the integral is performed.

Here we specify the previous expression to a rectangular flake of dimensions L_x and L_y, respectively, for which the properly normalized 2D exciton envelope function can be taken as $F_{exc}(x, y) = 1/\sqrt{L_x L_y}$, and assuming $f = 0.4$ eV^2 for a MoSe$_2$ thickness $d = 0.7$ nm as taken from the literature [42]. The electric field profile is then calculated with 3D-FDTD (a commercially

available software from Ansys-Lumerical was employed), as shown in Fig. 1(a), and only the in-plane components are assumed to contribute to the integral in Eq. (5). The latter is then reduced to $\int_0^{L_x} dx \int_0^{L_y} dy \left[|E_{\text{norm},x}| + |E_{\text{norm},y}| \right]$.

We numerically find that the maximal value of $\hbar g \simeq 5.1$ meV is obtained for a rectangular flake with $L_x = 5$ μm. Considering that the actual sample is shown to exhibit a partial coverage of the cavity region as well as a much more extended surface extension (Fig. 1), a reduced value may be expected. In fact, by calculating Eq. (5) for $L_x = 12$ μm and $L_y = 0.779$ μm, we obtain the theoretical value $\hbar g \simeq 4.2$ meV, which is qualitatively consistent with the experimentally determined one. The discrepancy arises from the independent estimate of the oscillator strength [42].

Appendix C: Avoided crossing

We include a plot demonstrating the subtle dispersive shift of the cavity as the exciton-cavity detuning is decreased (Fig. 6). The blue diagonal line tracks the peak of the neutral exciton photoluminescence in monolayer MoSe$_2$. The orange vertical line tracks what would be the temperature-independent cavity resonant frequency due to the low thermo-optic coefficient of silicon nitride. The curved purple line tracks the peak of the cavity transmission spectrum
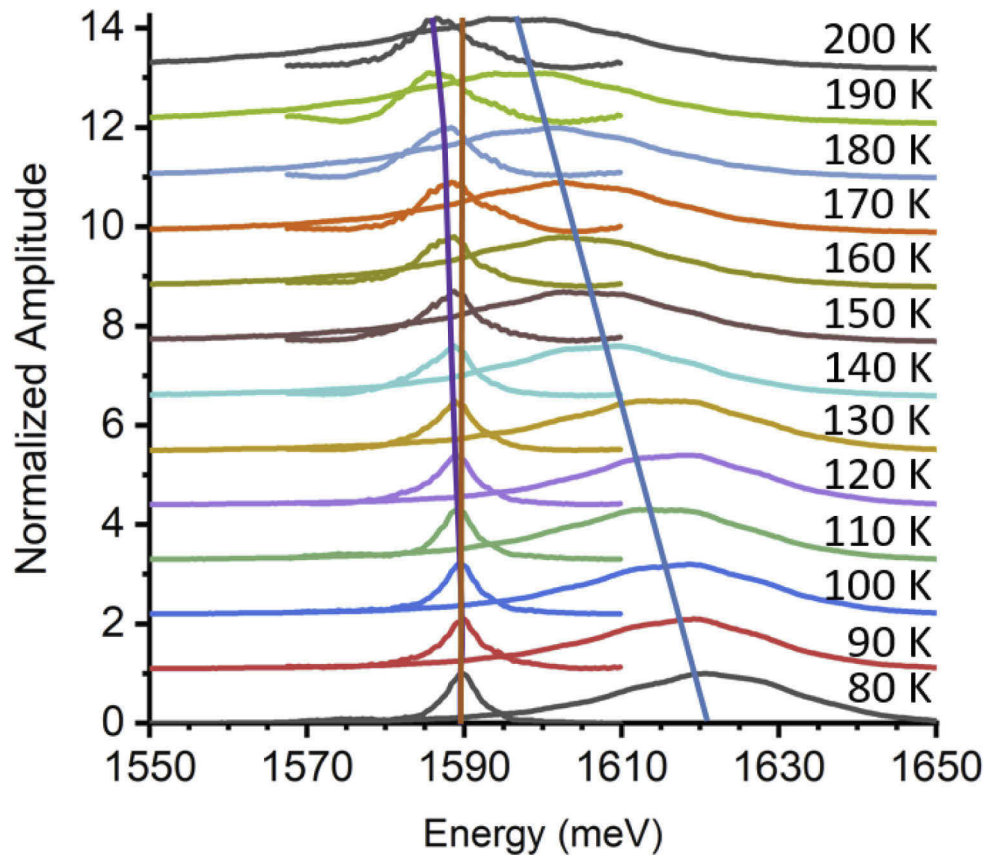

Fig. 6. Overlayed plots of the cavity transmission (left peak) and MoSe$_2$ photoluminescence (right peak). The center frequency of the neutral exciton exhibited in the photoluminescence is plotted in Fig. 3(a). The center frequency of the cavity resonance is plotted in Fig. 4(c) with respect to the exciton detuning from the bare cavity resonant frequency.

showing the avoided crossing of the cavity resonant frequency and the excitonic transition. The photoluminescence is the total emission of the monolayer flake. Should it be possible to observe the photoluminescent emission solely at the center of the cavity mode we would expect to see level repulsion of the exciton resonant frequency as well.

Disclosures. The authors declare no conflicts of interest.

Data availability. Data underlying the results presented in this paper are not publicly available at this time but may be obtained from the authors upon reasonable request.

References

1. C.-h. Liu, J. Zheng, Y. Chen, T. Fryett, and A. Majumdar, "Van der Waals materials integrated nanophotonic devices [Invited]," Opt. Mater. Express **9**(2), 384–399 (2019).
2. A. Verger, C. Ciuti, and I. Carusotto, "Polariton quantum blockade in a photonic dot," Phys. Rev. B **73**(19), 193306 (2006).
3. D. Zheng, S. Zhang, Q. Deng, M. Kang, P. Nordlander, and H. Xu, "Manipulating coherent plasmon–exciton interaction in a single silver nanorod on monolayer WSe$_2$," Nano Lett. **17**(6), 3809–3814 (2017).
4. J. Wen, H. Wang, W. Wang, Z. Deng, C. Zhuang, Y. Zhang, F. Liu, J. She, J. Chen, H. Chen, S. Deng, and N. Xu, "Room-temperature strong light–matter interaction with active control in single plasmonic nanorod coupled with two-dimensional atomic crystals," Nano Lett. **17**(8), 4689–4697 (2017).
5. M.-E. Kleemann, R. Chikkaraddy, E. M. Alexeev, D. Kos, C. Carnegie, W. Deacon, A. C. de Pury, C. Große, B. de Nijs, J. Mertens, A. I. Tartakovskii, and J. J. Baumberg, "Strong-coupling of WSe2 in ultra-compact plasmonic nanocavities at room temperature," Nat. Commun. **8**(1), 1296 (2017).
6. M. Wang, A. Krasnok, T. Zhang, L. Scarabelli, H. Liu, Z. Wu, L. M. Liz-Marzán, M. Terrones, A. Alù, and Y. Zheng, "Tunable Fano resonance and plasmon–exciton coupling in single Au Nanotriangles on monolayer WS$_2$ at room temperature," Adv. Mater. **30**(22), 1705779 (2018).
7. D. G. Angelakis, ed., *Quantum Simulations with Photons and Polaritons: Merging Quantum Optics with Condensed Matter Physics*, Quantum Science and Technology (Springer International Publishing, 2017).
8. D. Gerace, H. E. Türeci, A. Imamoglu, V. Giovannetti, and R. Fazio, "The quantum-optical Josephson interferometer," Nat. Phys. **5**(4), 281–284 (2009).
9. X. Liu, T. Galfsky, Z. Sun, F. Xia, E.-c. Lin, Y.-H. Lee, S. Kéna-Cohen, and V. M. Menon, "Strong light–matter coupling in two-dimensional atomic crystals," Nat. Photonics **9**(1), 30–34 (2015).
10. S. Dufferwiel, S. Schwarz, F. Withers, A. a. P. Trichet, F. Li, M. Sich, O. Del Pozo-Zamudio, C. Clark, A. Nalitov, D. D. Solnyshkov, G. Malpuech, K. S. Novoselov, J. M. Smith, M. S. Skolnick, D. N. Krizhanovskii, and A. I. Tartakovskii, "Exciton–polaritons in van der Waals heterostructures embedded in tunable microcavities," Nat. Commun. **6**(1), 8579 (2015).
11. X. Liu, W. Bao, Q. Li, C. Ropp, Y. Wang, and X. Zhang, "Control of coherently coupled exciton polaritons in monolayer tungsten disulphide," Phys. Rev. Lett. **119**(2), 027403 (2017).
12. C. Schneider, M. M. Glazov, T. Korn, S. Höfling, and B. Urbaszek, "Two-dimensional semiconductors in the regime of strong light-matter coupling," Nat. Commun. **9**(1), 2695 (2018).
13. Y. Chen, S. Miao, T. Wang, D. Zhong, A. Saxena, C. Chow, J. Whitehead, D. Gerace, X. Xu, S.-F. Shi, and A. Majumdar, "Metasurface integrated monolayer exciton polariton," Nano Lett. **20**(7), 5292–5300 (2020).
14. L. Zhang, R. Gogna, W. Burg, E. Tutuc, and H. Deng, "Photonic-crystal exciton-polaritons in monolayer semiconductors," Nat. Commun. **9**(1), 713 (2018).
15. V. Kravtsov, E. Khestanova, F. A. Benimetskiy, T. Ivanova, A. K. Samusev, I. S. Sinev, D. Pidgayko, A. M. Mozharov, I. S. Mukhin, M. S. Lozhkin, Y. V. Kapitonov, A. S. Brichkin, V. D. Kulakovskii, I. A. Shelykh, A. I. Tartakovskii, P. M. Walker, M. S. Skolnick, D. N. Krizhanovskii, and I. V. Iorsh, "Nonlinear polaritons in a monolayer semiconductor coupled to optical bound states in the continuum," Light: Sci. Appl. **9**(1), 56 (2020).
16. M. Sidler, P. Back, O. Cotlet, A. Srivastava, T. Fink, M. Kroner, E. Demler, and A. Imamoglu, "Fermi polaron-polaritons in charge-tunable atomically thin semiconductors," Nat. Phys. **13**(3), 255–261 (2017).

17. C. Gebhardt, M. Förg, H. Yamaguchi, I. Bilgin, A. D. Mohite, C. Gies, M. Florian, M. Hartmann, T. W. Hänsch, A. Högele, and D. Hunger, "Polariton hyperspectral imaging of two-dimensional semiconductor crystals," Sci. Rep. **9**(1), 13756 (2019).

18. A. Majumdar, A. Rundquist, M. Bajcsy, V. D. Dasika, S. R. Bank, and J. Vučković, "Design and analysis of photonic crystal coupled cavity arrays for quantum simulation," Phys. Rev. B **86**(19), 195312 (2012).

19. S. Wu, S. Buckley, J. R. Schaibley, L. Feng, J. Yan, D. G. Mandrus, F. Hatami, W. Yao, J. Vučković, A. Majumdar, and X. Xu, "Monolayer semiconductor nanocavity lasers with ultralow thresholds," Nature **520**(7545), 69–72 (2015).

20. Y. Li, J. Zhang, D. Huang, H. Sun, F. Fan, J. Feng, Z. Wang, and C. Z. Ning, "Room-temperature continuous-wave lasing from monolayer molybdenum ditelluride integrated with a silicon nanobeam cavity," Nat. Nanotechnol. **12**(10), 987–992 (2017).

21. C.-H. Liu, G. Clark, T. Fryett, S. Wu, J. Zheng, F. Hatami, X. Xu, and A. Majumdar, "Nanocavity integrated van der Waals heterostructure light-emitting tunneling diode," Nano Lett. **17**(1), 200–205 (2017).

22. T. K. Fryett, K. L. Seyler, J. Zheng, C.-H. Liu, X. Xu, and A. Majumdar, "Silicon photonic crystal cavity enhanced second-harmonic generation from monolayer WSe$_2$," 2D Mater. **4**(1), 015031 (2016).

23. X.-T. Gan, C.-Y. Zhao, S.-Q. Hu, T. Wang, Y. Song, J. Li, Q.-H. Zhao, W.-Q. Jie, and J.-L. Zhao, "Microwatts continuous-wave pumped second harmonic generation in few- and mono-layer GaSe," Light: Sci. Appl. **7**(1), 17126 (2018).

24. P. Rivera, T. K. Fryett, Y. Chen, C.-H. Liu, E. Ray, F. Hatami, J. Yan, D. Mandrus, W. Yao, A. Majumdar, and X. Xu, "Coupling of photonic crystal cavity and interlayer exciton in heterobilayer of transition metal dichalcogenides," 2D Mater. **7**(1), 015027 (2019).

25. Y. Liu, H. Fang, A. Rasmita, Y. Zhou, J. Li, T. Yu, Q. Xiong, N. Zheludev, J. Liu, and W. Gao, "Room temperature nanocavity laser with interlayer excitons in 2D heterostructures," Sci. Adv. **5**(4), eaav4506 (2019).

26. M. R. Molas, C. Faugeras, A. O. Slobodeniuk, K. Nogajewski, M. Bartos, D. M. Basko, and M. Potemski, "Brightening of dark excitons in monolayers of semiconducting transition metal dichalcogenides," 2D Mater. **4**(2), 021003 (2017).

27. T. K. Fryett, Y. Chen, J. Whitehead, Z. M. Peycke, X. Xu, and A. Majumdar, "Encapsulated silicon nitride nanobeam cavity for hybrid nanophotonics," ACS Photonics **5**(6), 2176–2181 (2018).

28. Y. Chen, J. Whitehead, A. Ryou, J. Zheng, P. Xu, T. Fryett, and A. Majumdar, "Large thermal tuning of a polymer-embedded silicon nitride nanobeam cavity," Opt. Lett. **44**(12), 3058–3061 (2019).

29. D. Rosser, T. Fryett, A. Ryou, A. Saxena, and A. Majumdar, "Exciton–phonon interactions in nanocavity-integrated monolayer transition metal dichalcogenides," npj 2D Mater. Appl. **4**(1), 20 (2020).

30. D. Rosser, D. Gerace, L. C. Andreani, and A. Majumdar, "Optimal condition to probe strong coupling of two-dimensional excitons and zero-dimensional cavity modes," arXiv:2107.00078 [cond-mat, physics:physics] (2021).

31. D. Rosser, T. Fryett, A. Saxena, A. Ryou, and A. Majumdar, "High-precision local transfer of van der Waals materials on nanophotonic structures," Opt. Mater. Express **10**(2), 645–652 (2020).

32. L. C. Andreani, G. Panzarini, and J.-M. Gérard, "Strong-coupling regime for quantum boxes in pillar microcavities: theory," Phys. Rev. B **60**(19), 13276–13279 (1999).

33. Q. Quan, P. B. Deotare, and M. Loncar, "Photonic crystal nanobeam cavity strongly coupled to the feeding waveguide," Appl. Phys. Lett. **96**(20), 203102 (2010).

34. K. Srinivasan and O. Painter, "Momentum space design of high-Q photonic crystal optical cavities," Opt. Express **10**(15), 670–684 (2002).

35. J. J. Olivero and R. L. Longbothum, "Empirical fits to the Voigt line width: a brief review," J. Quant. Spectrosc. Radiat. Transfer **17**(2), 233–236 (1977).

36. M. Selig, G. Berghäuser, A. Raja, P. Nagler, C. Schüller, T. F. Heinz, T. Korn, A. Chernikov, E. Malic, and A. Knorr, "Excitonic linewidth and coherence lifetime in monolayer transition metal dichalcogenides," Nat. Commun. **7**(1), 13279 (2016).

37. K. P. O'Donnell and X. Chen, "Temperature dependence of semiconductor band gaps," Appl. Phys. Lett. **58**(25), 2924–2926 (1991).

38. S. Tongay, J. Zhou, C. Ataca, K. Lo, T. S. Matthews, J. Li, J. C. Grossman, and J. Wu, "Thermally driven crossover from indirect toward direct bandgap in 2D semiconductors: MoSe$_2$ versus MoS$_2$," Nano Lett. **12**(11), 5576–5580 (2012).

39. S. Rudin, T. L. Reinecke, and B. Segall, "Temperature-dependent exciton linewidths in semiconductors," Phys. Rev. B **42**(17), 11218–11231 (1990).

40. J. Yang, H. Giessen, and P. Lalanne, "Simple analytical expression for the peak-frequency shifts of plasmonic resonances for sensing," Nano Lett. **15**(5), 3439–3444 (2015).

41. K. G. Cognée, W. Yan, F. L. China, D. Balestri, F. Intonti, M. Gurioli, A. F. Koenderink, and P. Lalanne, "Mapping complex mode volumes with cavity perturbation theory," Optica **6**(3), 269–273 (2019).

42. N. Lundt, A. Maryński, E. Cherotchenko, A. Pant, X. Fan, S. Tongay, G. Sęk, A. V. Kavokin, S. Höfling, and C. Schneider, "Monolayered MoSe2 : a candidate for room temperature polaritonics," 2D Mater. **4**(1), 015006 (2016).

43. A. Majumdar, A. Rundquist, M. Bajcsy, and J. Vučković, "Cavity quantum electrodynamics with a single quantum dot coupled to a photonic molecule," Phys. Rev. B **86**(4), 045315 (2012).

44. H. Deng, H. Haug, and Y. Yamamoto, "Exciton-polariton Bose-Einstein condensation," Rev. Mod. Phys. **82**(2), 1489–1537 (2010).

45. E. V. Denning, M. Wubs, N. Stenger, J. Mork, and P. T. Kristensen, "Quantum theory of two-dimensional materials coupled to electromagnetic resonators," arXiv:2103.14488 [cond-mat, physics:quant-ph] (2021).

46. H.-P. Breuer and F. Petruccione, *The Theory of Open Quantum Systems* (Oxford University Press, 2007).

47. K. Hennessy, A. Badolato, M. Winger, D. Gerace, M. Atatüre, S. Gulde, S. Fält, E. L. Hu, and A. Imamoğlu, "Quantum nature of a strongly coupled single quantum dot–cavity system," Nature **445**(7130), 896–899 (2007).

48. D. Englund, A. Faraon, I. Fushman, N. Stoltz, P. Petroff, and J. Vučković, "Controlling cavity reflectivity with a single quantum dot," Nature **450**(7171), 857–861 (2007).

49. F. P. Laussy, E. d. Valle, M. Schrapp, A. Laucht, and J. J. Finley, "Climbing the Jaynes-Cummings ladder by photon counting," J. Nanophotonics **6**(1), 061803 (2012).

50. L. C. Andreani, "Exciton-polaritons in bulk semiconductors and in confined electron and photon systems," in *Strong Light-Matter Coupling* (World Scientific, 2013), pp. 37–82.

51. O. A. Ajayi, J. V. Ardelean, G. D. Shepard, J. Wang, A. Antony, T. Taniguchi, K. Watanabe, T. F. Heinz, S. Strauf, X.-Y. Zhu, and J. C. Hone, "Approaching the intrinsic photoluminescence linewidth in transition metal dichalcogenide monolayers," 2D Mater. **4**(3), 031011 (2017).

52. J. G. Roch, N. Leisgang, G. Froehlicher, P. Makk, K. Watanabe, T. Taniguchi, C. Schönenberger, and R. J. Warburton, "Quantum-confined stark effect in a MoS_2 monolayer van der Waals heterostructure," Nano Lett. **18**(2), 1070–1074 (2018).

53. Y. Tang, J. Gu, S. Liu, K. Watanabe, T. Taniguchi, J. Hone, K. F. Mak, and J. Shan, "Tuning layer-hybridized moiré excitons by the quantum-confined Stark effect," Nat. Nanotechnol. **16**(1), 52–57 (2021).

54. J. Chen, X. Zhao, S. J. R. Tan, H. Xu, B. Wu, B. Liu, D. Fu, W. Fu, D. Geng, Y. Liu, W. Liu, W. Tang, L. Li, W. Zhou, T. C. Sum, and K. P. Loh, "Chemical vapor deposition of large-size monolayer $MoSe_2$ crystals on molten glass," J. Am. Chem. Soc. **139**(3), 1073–1076 (2017).

55. F. Liu, W. Wu, Y. Bai, S. H. Chae, Q. Li, J. Wang, J. Hone, and X.-Y. Zhu, "Disassembling 2D van der Waals crystals into macroscopic monolayers and reassembling into artificial lattices," Science **367**(6480), 903–906 (2020).

56. Q. Quan and M. Loncar, "Deterministic design of wavelength scale, ultra-high Q photonic crystal nanobeam cavities," Opt. Express **19**(19), 18529–18542 (2011).

57. R. Khelifa, P. Back, N. Flöry, S. Nashashibi, K. Malchow, T. Taniguchi, K. Watanabe, A. Jain, and L. Novotny, "Coupling interlayer excitons to whispering gallery modes in van der Waals heterostructures," Nano Lett. **20**(8), 6155–6161 (2020).

58. C. Qian, V. Villafane, P. Soubelet, A. Hötger, T. Taniguchi, K. Watanabe, N. P. Wilson, A. V. Stier, A. W. Holleitner, and J. J. Finley, "Strong coupling and non-local interactions in MoS_2 monolayers coupled to high-Q nanocavities," arXiv:2107.04387 [cond-mat] (2021).

59. S. G. Johnson and J. D. Joannopoulos, "Block-iterative frequency-domain methods for Maxwell's equations in a planewave basis," Opt. Express **8**(3), 173–190 (2001).